Article

https://doi.org/10.1038/s41565-023-01324-3

Hyperbolic whispering-gallery phonon polaritons in boron nitride nanotubes

Xiangdong Guo[1,2,10], Ning Li[3,10], Xiaoxia Yang[1,2] ✉, Ruishi Qi[3], Chenchen Wu[1,2], Ruochen Shi[3], Yuehui Li[3], Yang Huang[4], F. Javier García de Abajo[5,6] ✉, En-Ge Wang[7,8,9], Peng Gao[3,7] ✉ & Qing Dai[1,2] ✉

Light confinement in nanostructures produces an enhanced light–matter interaction that enables a vast range of applications including single-photon sources, nanolasers and nanosensors. In particular, nanocavity-confined polaritons display a strongly enhanced light–matter interaction in the infrared regime. This interaction could be further boosted if polaritonic modes were moulded to form whispering-gallery modes; but scattering losses within nanocavities have so far prevented their observation. Here, we show that hexagonal BN nanotubes act as an atomically smooth nanocavity that can sustain phonon-polariton whispering-gallery modes, owing to their intrinsic hyperbolic dispersion and low scattering losses. Hyperbolic whispering-gallery phonon polaritons on BN nanotubes of ~4 nm radius (sidewall of six atomic layers) are characterized by an ultrasmall nanocavity mode volume ($V_m \approx 10^{-10}\lambda_0^3$ at an optical wavelength $\lambda_0 \approx 6.4$ μm) and a Purcell factor (Q/V_m) as high as 10^{12}. We posit that BN nanotubes could become an important material platform for the realization of one-dimensional, ultrastrong light–matter interactions, with exciting implications for compact photonic devices.

The light–matter interaction is the basis of optics, where it has fuelled a long list of breakthrough applications, including nanolasers[1,2], nano-biosensors[3–5], enhanced optical nonlinearities[6,7] and the exploration of cavity quantum electrodynamics[8–10]. Consequently, the discovery of novel light confinement regimes is vital to further enhance light–matter interactions[11–13], whose strength can be quantified by the dimensionless Purcell factor ~Q/V_m (refs. [14–17]), approximated as the ratio of the quality factor Q to the mode volume $V_m = V/\lambda_0^3$ (normalized using the light wavelength λ_0; V is optical volume)[18–20]. Therefore, exploring optical modes with an elevated Q and ultrasmall mode volume provides a route to increasing the Purcell factor for enhancing light–matter interactions.

Optical cavities can trap light based on geometry to host whispering-gallery modes with high quality factors ($Q \approx 10^8$)[21,22], but this comes at the expense of large mode volumes. Plasmon modes associated with collective electron oscillations at material surfaces

[1]CAS Key Laboratory of Nanophotonic Materials and Devices, CAS Key Laboratory of Standardization and Measurement for Nanotechnology, CAS Center for Excellence in Nanoscience, National Center for Nanoscience and Technology, Beijing, China. [2]Center of Materials Science and Optoelectronics Engineering, University of Chinese Academy of Sciences, Beijing, China. [3]International Center for Quantum Materials, Electron Microscopy Laboratory, School of Physics, Academy for Advanced Interdisciplinary Studies, Interdisciplinary Institute of Light-Element Quantum Materials and Research Center for Light-Element Advanced Materials, Peking University, Beijing, China. [4]School of Materials Science and Engineering, Hebei Key Laboratory of Boron Nitride Micro and Nano Materials, Hebei University of Technology, Tianjin, China. [5]ICFO-Institut de Ciencies Fotoniques, The Barcelona Institute of Science and Technology, Castelldefels (Barcelona), Spain. [6]ICREA-Institució Catalana de Recerca i Estudis Avançats, Barcelona, Spain. [7]Collaborative Innovation Center of Quantum Matter, Beijing, China. [8]Songshan Lake Materials Lab, Institute of Physics, Chinese Academy of Sciences, Guangdong, China. [9]School of Physics, Liaoning University, Shenyang, China. [10]These authors contributed equally: Xiangdong Guo, Ning Li. ✉e-mail: yangxx@nanoctr.cn; javier.garciadeabajo@nanophotonics.es; p-gao@pku.edu.cn; daiq@nanoctr.cn

https://doi.org/10.1038/s41565-023-01324-3

can greatly compress light into nanoscale volumes, but their quality factors are substantially smaller ($Q < 10^2$)[23,24] because of intrinsic losses. As a compromise between these two extreme regimes, the coupling of plasmons to dielectric nanocavities to form whispering-gallery modes constitutes a promising pathway to improve the Purcell factor[25,26], although the trade-off between mode volume and quality factor is still limited by intrinsic losses in the plasmon-supporting materials[18,27–29].

Like plasmons, phonon polaritons in hexagonal BN (hBN) possess a bosonic nature, but they exhibit much lower intrinsic losses[30–33] and display isofrequency curves[34–36] of hyperbolic morphology that can supply the large wave vectors that are necessary for mode confinement down to ultrasmall nanocavities. We thus expect hyperbolic whispering-gallery phonon polaritons (HWG-PhPs) with an ultrahigh Purcell factor to be enabled when wrapping a hBN film into a hBN nanotube (BNNT).

Guided by this intuition, in this work we experimentally demonstrate ultra-confined HWG-PhP modes propagating around the wall of BNNTs by means of electron energy-loss spectroscopy (EELS). The quality factors of HWG-PhP modes, measured on the same samples by using the atomic force microscopy (AFM)-based infrared spectroscopy (AFM-IR) technique, can reach values as high as ~220 because of the absence of scattering channels in the seamless atomically smooth nanocavities. HWG-PhP modes can be sustained on a ~4-nm-radius (sidewall of six atomic layers) BNNT, which exhibits an ultrasmall volume $V_m \approx 10^{-10}$, leading to an ultrahigh Purcell factor $Q/V_m \approx 10^{12}$. Our work supports HWG-PhP modes on nanotubes as a powerful platform to realize record-high Purcell factors, thus offering a paradigm for applications in compact nanophotonic devices, such as nanosensors, nanolasers and optical filters.

Prediction and observation of HWG-PhP modes in a single BNNT

Multi-walled BNNTs constitute atomically smooth nanocavities, as illustrated by a six-layer BNNT in Fig. 1a (high-resolution transmission electron microscopy (TEM) image). In this work, BNNTs were grown by chemical vapour deposition (details in the Methods) and with various radii (Supplementary Fig. 1). These BNNTs can be regarded as a sheet of hBN being rolled into tubular geometries that inherit the hyperbolic phonon-polariton dispersion of hBN (details in Supplementary Note 1 and Supplementary Fig. 2). Since hyperbolic isofrequency curves are unbound in the wave vector (in contrast to isotropic materials, which typically display bound spherical or elliptical isofrequency curves), the propagation or interference resonances of a high wave vector can be supported on ultrasmall hBN structures. Notably, since the wave vector of the HWG-PhP mode of a BNNT is much smaller than $1/d$ ($1/d > 20{,}000k_0$, with d being the out-of-plane atomic layer spacing and k_0 being the free-space wavevector), the effective permittivity of the tube does not require non-local corrections[37,38]. Thus, the long-range propagation of highly confined hyperbolic rays on a hBN film can form the sought-after whispering-gallery modes on a BNNT, as shown in Fig. 1b. The detected HWG-PhP modes are also the fundamental azimuthal resonance modes. The mode can be observed in frequency space with an ultra-sensitive spatially resolved spectroscopy technique. The spectra of hyperbolic phonon polaritons in BNNTs with different axis lengths (L = 150 and 300 nm) are predicted by the theoretical simulations shown in Fig. 1c. These peaks can be recognized as two types of phonon polaritons: Fabry–Perot (FP) cavity modes and HWG-PhP modes in the high-frequency range. As FP modes resonate along the longitudinal axis, their peak frequencies are shifted with the length of the BNNT. By contrast, HWG-PhP modes propagate around the circular wall of the tube and are thus independent of the tube length. We conclude that the high-frequency peak indicates that there is a HWG-PhP mode confined to the tube nanocavity.

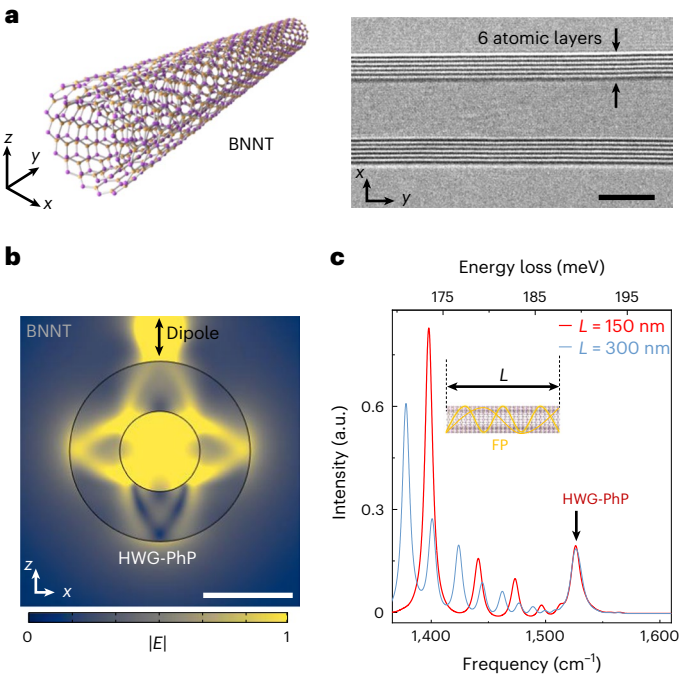

Fig. 1 | HWG-PhPs in a single BNNT. a, Schematic diagram of a one-dimensional BNNT and TEM image. BNNTs are composed of several atomic layers, such as the six-walled tube shown in the image. The scale bar is 5 nm. **b**, Near-field distribution dominated by hyperbolic whispering-gallery polaritons in a BNNT. The excitation source is a radially oriented dipole (double black arrow). E is the electric field. The scale bar is 4 nm. **c**, Simulated EELS spectra of one-dimensional BNNT hyperbolic whispering-gallery modes for two different tube lengths, L. FP modes (left features below ~1515 cm^{-1}, and scheme in the inset) vary with L, in contrast to the HWG-PhP modes (right feature above ~1515 cm^{-1}).

To directly observe deep subwavelength HWG-PhP modes in a single BNNT, we employ the AFM-IR technique[39–41]. It is an effective optical means to measure nano-infrared (nanoIR) signals, which combines the spatial resolution of AFM with the specificity of absorption spectroscopy (shown in Fig. 2a; details in the Methods)[42,43]. In Fig. 2b, the nanoIR signals of hyperbolic phonon polaritons (HPhPs) at different spatial positions on a BNNT are characterized by AFM-IR (tube radius R = 18 nm; details in Supplementary Fig. 3). The spectra from three points reveal a fixed resonance peak at 190 meV (~1,530 cm^{-1}, indicated by the black arrow in Fig. 2b), stemming from vibrations along the radial direction that are insensitive to the position along the axis of the BNNT. In addition, this resonance mode can be detected in BNNTs with different radii (Supplementary Fig. 3) and is in good agreement with the theoretically predicted HWG-PhP mode in Fig. 1c.

Scattering-type scanning near-field optical microscopy (s-SNOM[30,44]; details in the Methods) is employed to investigate the intensity distribution of resonance modes on the same BNNT in real space. The interference patterns in Fig. 2c are generated along the axis of the BNNT, corresponding to the longitudinal FP resonance mode at 1,480 cm^{-1}. Notably, the longitudinal FP modes of BNNTs have also been observed in previous s-SNOM works demonstrating imaging and dispersion mapping of such one-dimensional excitations[45–49]. In our experiment, this interference pattern is reshaped from the centre to the sidewalls as the resonance frequency is varied from 1,480 to 1,530 cm^{-1} (Fig. 2d and the full evolution in Supplementary Fig. 4). From the electromagnetic field intensity distribution extracted along the transverse x direction of the BNNT (grey curves in Fig. 2c,d), the HWG-PhP mode is shown to display two peaks, while the FP mode presents only one peak (details of feature analysis in Supplementary

https://doi.org/10.1038/s41565-023-01324-3

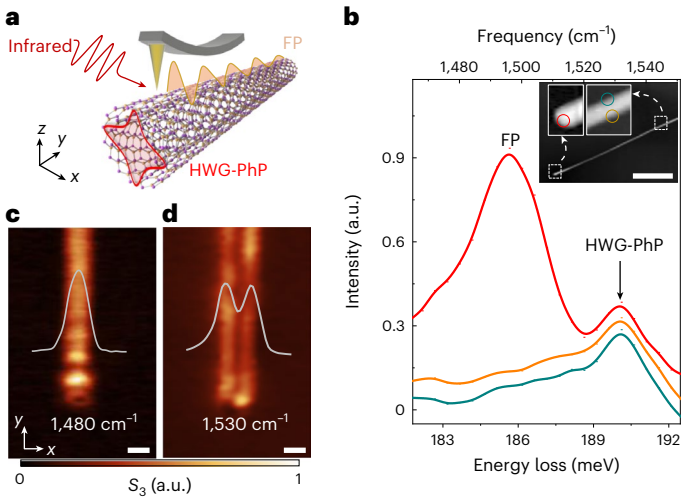

Fig. 2 | Direct observation of HWG-PhP modes. a, Schematic diagram of AFM-probe-based near-field characterization of a single BNNT. **b**, Measured nanoIR signals of hyperbolic polaritons obtained by AFM-IR at different spatial positions of a single BNNT. The inset AFM image illustrates the morphology of the BNNT, with the two additional insets showing zoomed-in views. The scale bar is 3 µm. **c**,**d**, Near-field two-dimensional distributions of the s-SNOM signal (normalized amplitude S_3) at different frequencies: 1,480 cm^{-1} (**c**) and 1,530 cm^{-1} (**d**). Cuts of the near-field intensity distributions along the diameter of the BNNT are superimposed as grey line profiles. The scale bars are 100 nm.

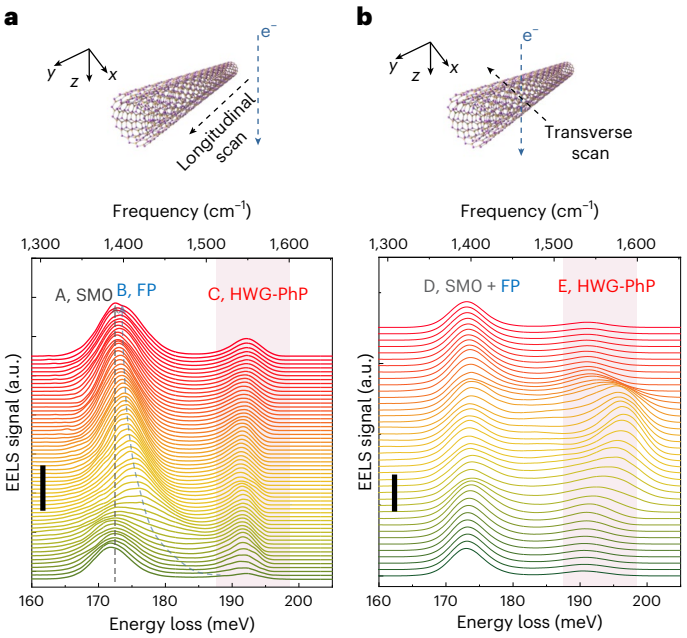

Fig. 3 | EELS quantitative characterization of HWG-PhP modes. a,**b**, A series of EELS spectra obtained as the e-beam is scanned either along the axis of an individual BNNT (**a**; longitudinal scan in y from 0 (tube edge) to 500 nm (tube centre), with x = 42 nm in aloof configuration; the vertical black scale bar indicates 100 nm) or perpendicular to the axis (**b**; transverse scan in x from −54 to 54 nm, with y = 500 nm; the scale bar indicates 20 nm). The BNNT has an outer radius $R \approx 36$ nm and an inner radius $r \approx 13$ nm. The pink-shaded areas highlight the HWG-PhP modes. Grey and blue dashed lines in the bottom panel of **a** are guides for the eye indicating the peak shifts of A and B, respectively. The SM0 mode and FP mode are also marked. The upper panels show the e-beam (e$^-$; downward blue arrows) and scanning (dashed black arrows) directions.

Fig. 4). We stress that the separation between the two peaks is much larger than the BNNT diameter (about 36 nm). This broadening in the horizontal width of the s-SNOM images is due to the effect of the finite size and round shape of the tip in the s-SNOM experiments, similar to those in AFM measurements[50]. This interference pattern at 1,530 cm^{-1} is consistent with the predicted near-field distribution of a HWG-PhP in Fig.1b, which is another piece of solid evidence that an HWG-PhP mode is supported on a BNNT.

Quantitative dispersion of HWG-PhP modes

The HWG-PhP mode on BNNTs has been identified using near-field optics techniques with resonant spectra and a near-field distribution. To further analyse its dispersion relation, which is highly correlated with the geometry of the nanocavity formed by BNNTs, monochromatic EELS incorporated in a scanning TEM (STEM) with angstrom spatial resolution is employed (details in Methods). Polariton signals can be characterized by scanning the electron beam (e-beam) over the spatial extension of the sample in the EELS experiment. Thus, we perform systematic STEM–EELS measurements by moving the e-beam along directions parallel (longitudinal) and perpendicular (transverse) with respect to the axis of the BNNT, as schematically illustrated in Fig. 3a,b. Under aloof excitation (that is, with the e-beam passing close to but outside of the BNNT)[51], only HPhP modes are excited, resulting in distinct peaks in the STEM–EELS spectra (Supplementary Note 2 and Supplementary Fig. 5), while both HPhP and longitudinal optical (LO)-phonon signals are detected for bulk excitation (that is, with the e-beam traversing the BNNT). To understand the observed spectral features, we perform finite-element-method simulations of the STEM–EELS spectra (details in the Methods and Supplementary Fig. 6), which are in good agreement with the respective experimental spectra (Fig. 3a,b).

In the longitudinal scan of the e-beam (Fig. 3a), the observed resonant features (A, B and C peaks from lower to higher frequency) are HPhP modes under aloof excitation, similar to those in nanoflakes[51–53], but strongly modified by the geometry of the BNNT. As the e-beam is moved from the edge to the centre of the nanotube along the transverse direction, the frequencies of peaks A (~172 meV) and C (~193 meV) remain almost unchanged, while peak B (~172–193 meV) is monotonically redshifted. The intensities of peak B strongly depend on the e-beam position because the excited HPhPs propagate along the BNNT towards the ends, where they are reflected, thus producing a characteristic interference pattern. This behaviour clearly points to a spectrally evolving standing wave (that is, a longitudinal HPhP mode), similar to HPhP resonances in hBN rods[54]. Thus, peak B can be regarded as a longitudinal FP-cavity resonant mode. In addition, peak B merges with peak A as the e-beam moves to the middle of the nanotube, implying that peak A originates from the fundamental surface HPhP mode (SM0) in the BNNT. By contrast, the signal of peak C (Fig. 3a) stems from the highest-frequency feature before broadening due to the finite instrument resolution (Supplementary Fig. 6). Peak C exceeds the frequency limit of the longitudinal FP modes and is not affected by the BNNT length (Supplementary Fig. 7); therefore, it is a HWG-PhP mode.

The transverse scan of the e-beam, in the middle of the longitudinal axial length of the BNNT, provides further insight into the HWG-PhP modes. In the aloof excitation region, the two observed peaks (D and E from lower to higher frequency in Fig. 3b) can be ascribed to the SM0 + FP and HWG-PhP modes. In the bulk excitation region, the SM0 + FP mode remains unchanged, while the high-frequency peak (HWG-PhP) shifts to blue as the e-beam moves into the inner region of the BNNT. As expected, the transverse scan renders symmetric results with respect to the nanotube axis. Such behaviour indicates a spectrally evolving standing wave pattern along the radial direction associated with the HWG-PhP modes of the BNNT.

According to the analysis presented above, narrow BNNTs are predicted to have HWG-PhP modes with reduced mode volume.

https://doi.org/10.1038/s41565-023-01324-3

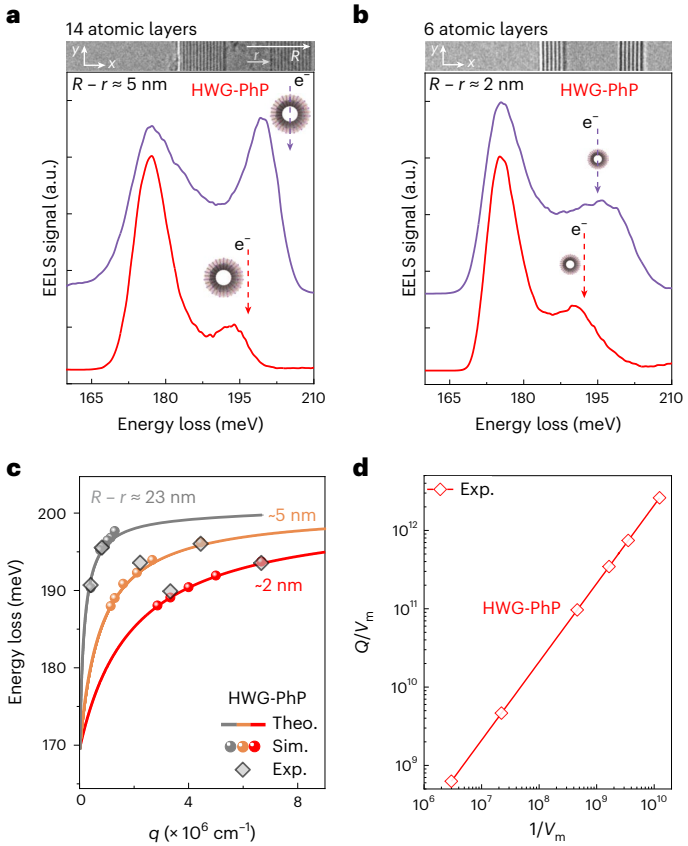

Fig. 4 | Dispersion and V_m confinement of HWG-PhP modes in few-layer BNNTs. a,b, HWG-PhP modes supported by ultrathin individual BNNTs consisting of 14 atomic layers (**a**; outer radius, $R \approx 7$ nm; outer minus inner radii, $R - r \approx 5$ nm) and 6 atomic layers ($R \approx 4$ nm, $R - r \approx 2$ nm). **c**, Dispersion relation of HWG-PhP modes in BNNTs of different sidewall thicknesses, $R - r$, of 23 nm, 5 nm and 2 nm. r represents the inner radius of BNNT. Solid curves, theoretical model calculations (Theo.); diamonds, measured EELS data from Figs. 3 and 4a,b and Supplementary Fig. 9 (Exp.); circles, numerical simulations from Supplementary Figs. 7, 8 and 10 (Sim.). **d**, Ratio Q/V_m (proportional to the Purcell factor) as a function of normalized mode volume V_m for HWG-PhP modes in BNNTs based on experimental data points extracted from Figs. 3 and 4a,b and Supplementary Fig. 9.

In experiments, HWG-PhP modes are observed on BNNTs down to 14 atomic layers ($R \approx 7$ nm) and 6 atomic layers ($R \approx 4$ nm; Fig. 4a,b). At this atomic scale, the intensities of HWG-PhP modes become gradually weaker as the sidewall thickness decreases. For a sidewall thickness below six atomic layers, the HWG-PhP mode is difficult to resolve in the EELS spectra.

As the electromagnetic energy of the HWG-PhP modes is mainly distributed inside the BNNT, its dispersion relation can be derived in analogy to volume-confined HPhP modes in hBN films, which follow the analytical expression[30] $q(\omega) + ik(\omega) = -\frac{2\psi}{d}\arctan\left(\frac{\varepsilon_0}{\psi}\right)$, where q and k are the real and imaginary parts of the HPhP wave vector; ω is the frequency; ε_0 is the free-space permittivity; the ratio $\psi = \sqrt{\varepsilon_\parallel}/i\sqrt{\varepsilon_\perp}$ involves the dielectric function of the BNNT along the tangential ($\varepsilon_\parallel$) and radial ($\varepsilon_\perp$) directions; and d is the sidewall thickness $R - r$. In the experiment, multiple sets of EELS spectra for BNNTs with sidewall thicknesses of 23 nm, 5 nm and 2 nm were measured and are presented in Fig. 3 and Supplementary Figs. 8 and 9. In particular, the wavelength of the HWG-PhP mode has a twofold difference when the e-beam hits the middle or the outer side of the BNNT (details in Supplementary Fig. 8). Therefore, the wavelength and resonance frequency of the HWG-PhP mode can be clearly extracted. The points corresponding to measured HWG-PhP modes in the frequency versus wave vector diagram (diamonds in Fig. 4c) are extracted from the EELS data in Figs. 3 and 4a,b. The simulated EELS spectra for a series of BNNTs with different radii and sidewall thicknesses (Supplementary Figs. 10–12) are calculated and then plotted as circles in Fig. 4c.

Ultrasmall mode volume of HWG-PhP modes

According to the dispersion relation in Fig. 4c, HWG-PhP modes in BNNTs exhibit strong wavelength compression and enhanced optical fields, and in particular, the ultrasmall normalized mode volume V_m (refs. [18,19,55]) can be calculated as $V_m = \lambda_{HWG\text{-}PhP}{}^3/4\pi^2\lambda_0{}^3$ ($\lambda_{HWG\text{-}PhP}$ is the wavelength of HWG-PhP, details of the confined mode in Supplementary Fig. 13). Therefore, the HWG-PhP mode on the ~4-nm-radius BNNT can have an ultrasmall normalized mode volume on the order of ~10^{-10}. Thanks to the atomic smoothness of BNNT nanocavities, the damping of the HWG-PhP modes is dominated by intrinsic propagation loss, as we show in Supplementary Note 3 and Supplementary Fig. 14. The actual loss rate γ of HWG-PhP modes is measured by nanoIR spectroscopy ($\gamma \approx 7$–8 cm^{-1}) in Supplementary Fig. 14. The quality factor of HWG-PhPs (~220) can be derived from its definition $Q = \omega_{res}/\gamma$, where ω_{res} is the resonance frequency. Remarkably, the damping rates remain unchanged for BNNTs with different radii and sidewall thicknesses, as losses in the HWG-PhP modes mainly originate from intrinsic inelastic transitions in the material. Therefore, the quality factors for BNNTs with radii of ~7 nm and 4 nm are well assessed in our experiment by averaging the measured quality factors ($\bar{Q} \approx 210$) below 1,580 cm^{-1} in Supplementary Fig. 14. Based on these experimental values of Q and V_m, the Purcell factor Q/V_m of HWG-PhP modes can reach ~10^{12}, revealing a high level of the local density of optical states (Fig. 4d; more details in Supplementary Notes 4 and 5). In addition, the existence of whispering-gallery modes in an artificial hyperbolic plasmonic metamaterial (with a repetition of Ag and dielectric layers) has been theoretically predicted[56] and predicted to exhibit an extremely high local density of optical states reaching a value of ~10^6.

These extraordinary characteristics of HWG-PhPs are a consequence of both the intrinsic material properties and the one-dimensional nanocavity geometry. BNNTs constitute natural atomically smooth nanocavities with negligible scattering loss, as well as the hyperbolicity of their polaritons inherited from the base material, hBN. Because of these unique properties, HWG-PhP modes in BNNTs can overcome the trade-off between mode volume and quality factor. In addition, these characteristics are ideal to maintain an excellent level of quantum coherence, thus providing a promising platform for realizing single-photon sources for quantum information applications.

Conclusions

In conclusion, we directly observe HWG-PhP modes in BNNTs by both AFM-IR and STEM–EELS with quality factors up to ~220. These whispering-gallery modes are formed by confining phonon polaritons into atomically smooth cylindrical nanocavities (the BNNTs)—an effect that is made possible by the hyperbolicity and ensuing boundless wave vectors of phonon polaritons. Moreover, we demonstrate that HWG-PhP modes can be sustained on a ~4-nm-radius BNNT, which exhibits an ultrasmall volume $V_m \approx 10^{-10}$ and thus reveals an unprecedented level of the local density of optical states leading to an ultrahigh Purcell factor of $Q/V_m \approx 10^{12}$. Our study provides a new paradigm for nanophotonics based on one-dimensional-nanomaterial polaritons, revealing extraordinarily strong light–matter interaction capabilities and holding great potential for long-sought-after applications in quantum nanophotonics.

Online content

Any methods, additional references, Nature Portfolio reporting summaries, source data, extended data, supplementary information, acknowledgements, peer review information; details of author contributions

and competing interests; and statements of data and code availability are available at https://doi.org/10.1038/s41565-023-01324-3.

References

1. Oulton, R. F. et al. Plasmon lasers at deep subwavelength scale. *Nature* **461**, 629–632 (2009).
2. Wang, Y. et al. Stable, high-performance sodium-based plasmonic devices in the near infrared. *Nature* **581**, 401–405 (2020).
3. Rodrigo, D. et al. Mid-infrared plasmonic biosensing with graphene. *Science* **349**, 165–168 (2015).
4. Stockman, M. I. Nanoplasmonic sensing and detection. *Science* **348**, 287–288 (2015).
5. Tittl, A. et al. Imaging-based molecular barcoding with pixelated dielectric metasurfaces. *Science* **360**, 1105–1109 (2018).
6. Sivis, M. et al. Tailored semiconductors for high-harmonic optoelectronics. *Science* **357**, 303–306 (2017).
7. Zasedatelev, A. V. et al. Single-photon nonlinearity at room temperature. *Nature* **597**, 493–497 (2021).
8. Yoo, D. et al. Ultrastrong plasmon–phonon coupling via epsilon-near-zero nanocavities. *Nat. Photon.* **15**, 125–130 (2021).
9. Mirhosseini, M. et al. Cavity quantum electrodynamics with atom-like mirrors. *Nature* **569**, 692–697 (2019).
10. Wang, K. et al. Coherent interaction between free electrons and a photonic cavity. *Nature* **582**, 50–54 (2020).
11. Rivera, N. & Kaminer, I. Light–matter interactions with photonic quasiparticles. *Nat. Rev. Phys.* **2**, 538–561 (2020).
12. Forn-Díaz, P., Lamata, L., Rico, E., Kono, J. & Solano, E. Ultrastrong coupling regimes of light-matter interaction. *Rev. Mod. Phys.* **91**, 025005 (2019).
13. Kfir, O. et al. Controlling free electrons with optical whispering-gallery modes. *Nature* **582**, 46–49 (2020).
14. Agio, M. & Cano, D. M. The Purcell factor of nanoresonators. *Nat. Photon.* **7**, 674–675 (2013).
15. Min, B. et al. High-*Q* surface-plasmon-polariton whispering-gallery microcavity. *Nature* **457**, 455–458 (2009).
16. Yao, J., Yang, X., Yin, X., Bartal, G. & Zhang, X. Three-dimensional nanometer-scale optical cavities of indefinite medium. *Proc. Natl Acad. Sci. USA* **108**, 11327–11331 (2011).
17. Su, Y., Chang, P., Lin, C. & Helmy, A. Record Purcell factors in ultracompact hybrid plasmonic ring resonators. *Sci. Adv.* **5**, eaav1790 (2019).
18. Alcaraz Iranzo, D. et al. Probing the ultimate plasmon confinement limits with a van der Waals heterostructure. *Science* **360**, 291–295 (2018).
19. Epstein, I. et al. Far-field excitation of single graphene plasmon cavities with ultracompressed mode volumes. *Science* **368**, 1219–1223 (2020).
20. Alfaro-Mozaz, F. J. et al. Deeply subwavelength phonon-polaritonic crystal made of a van der Waals material. *Nat. Commun.* **10**, 42 (2019).
21. Long, J. C. et al. Upper limits to submillimetre-range forces from extra space-time dimensions. *Nature* **421**, 922–925 (2003).
22. Vahala, K. J. Optical microcavities. *Nature* **424**, 839–846 (2003).
23. Jiang, N., Zhuo, X. & Wang, J. Active plasmonics: principles, structures, and applications. *Chem. Rev.* **118**, 3054–3099 (2018).
24. Lee, I.-H., Yoo, D., Avouris, P., Low, T. & Oh, S.-H. Graphene acoustic plasmon resonator for ultrasensitive infrared spectroscopy. *Nat. Nanotechnol.* **14**, 313–319 (2019).
25. Cho, C. H. et al. Tailoring hot-exciton emission and lifetimes in semiconducting nanowires via whispering-gallery nanocavity plasmons. *Nat. Mater.* **10**, 669–675 (2011).
26. Cho, C. H., Aspetti, C. O., Park, J. & Agarwal, R. Silicon coupled with plasmon nanocavity generates bright visible hot-luminescence. *Nat. Photon.* **7**, 285–289 (2013).
27. Yan, H. et al. Damping pathways of mid-infrared plasmons in graphene nanostructures. *Nat. Photon.* **7**, 394–399 (2013).
28. Lee, I. H. et al. Image polaritons in boron nitride for extreme polariton confinement with low losses. *Nat. Commun.* **11**, 3649 (2020).
29. Lundeberg, M. B. et al. Tuning quantum nonlocal effects in graphene plasmonics. *Science* **357**, 187–191 (2017).
30. Dai, S. et al. Tunable phonon polaritons in atomically thin van der Waals crystals of boron nitride. *Science* **343**, 1125–1129 (2014).
31. Giles, A. J. et al. Ultralow-loss polaritons in isotopically pure boron nitride. *Nat. Mater.* **17**, 134–139 (2018).
32. Basov, D. N., Fogler, M. M. & Garcia de Abajo, F. J. Polaritons in van der Waals materials. *Science* **354**, aag1992 (2016).
33. Low, T. et al. Polaritons in layered two-dimensional materials. *Nat. Mater.* **16**, 182–194 (2017).
34. Guddala, S. et al. Topological phonon-polariton funneling in midinfrared metasurfaces. *Science* **374**, 225–227 (2021).
35. Caldwell, J. D. et al. Photonics with hexagonal boron nitride. *Nat. Rev. Mater.* **4**, 552–567 (2019).
36. Jacob, Z. Nanophotonics: hyperbolic phonon-polaritons. *Nat. Mater.* **13**, 1081–1083 (2014).
37. Yuan, Z. et al. Extremely confined acoustic phonon polaritons in monolayer-hBN/metal heterostructures for strong light–matter interactions. *ACS Photon.* **7**, 2610–2617 (2020).
38. Rivera, N., Christensen, T. & Narang, P. Phonon polaritonics in two-dimensional materials. *Nano Lett.* **19**, 2653–2660 (2019).
39. Lu, F., Jin, M. & Belkin, M. A. Tip-enhanced infrared nanospectroscopy via molecular expansion force detection. *Nat. Photon.* **8**, 307–312 (2014).
40. Ambrosio, A. et al. Mechanical detection and imaging of hyperbolic phonon polaritons in hexagonal boron nitride. *ACS Nano* **11**, 8741–8746 (2017).
41. Wang, L. et al. Revealing phonon polaritons in hexagonal boron nitride by multipulse peak force infrared microscopy. *Adv. Opt. Mater.* **8**, 1901084 (2019).
42. Brown, L. V. et al. Nanoscale mapping and spectroscopy of nonradiative hyperbolic modes in hexagonal boron nitride nanostructures. *Nano Lett.* **18**, 1628–1636 (2018).
43. Guo, M. et al. Toroidal polar topology in strained ferroelectric polymer. *Science* **371**, 1050–1056 (2021).
44. Li, P. et al. Infrared hyperbolic metasurface based on nanostructured van der Waals materials. *Science* **359**, 892–896 (2018).
45. Xu, X. G. et al. Mid-infrared polaritonic coupling between boron nitride nanotubes and graphene. *ACS Nano* **8**, 11305–11312 (2014).
46. Xu, X. G. et al. One-dimensional surface phonon polaritons in boron nitride nanotubes. *Nat. Commun.* **5**, 4782 (2014).
47. Phillips, C., Lai, Y. F. & Walker, G. C. Fabry–Perot phonon polaritons in boron nitride nanotube resonators. *J. Phys. Chem. Lett.* **12**, 11683–11687 (2021).
48. Wagner, M. et al. Ultrabroadband nanospectroscopy with a laser-driven plasma source. *ACS Photon.* **5**, 1467–1475 (2018).
49. Jiang, J. H., Xu, X. G., Gilburd, L. & Walker, G. C. Optical hot-spots in boron-nitride nanotubes at mid infrared frequencies: one-dimensional localization due to random-scattering. *Opt. Express* **25**, 25059–25070 (2017).
50. Flater, E. E., Zacharakis-Jutz, G. E., Dumba, B. G., White, I. A. & Clifford, C. A. Towards easy and reliable AFM tip shape determination using blind tip reconstruction. *Ultramicroscopy* **146**, 130–143 (2014).

51. Li, N. et al. Direct observation of highly confined phonon polaritons in suspended monolayer hexagonal boron nitride. *Nat. Mater.* **20**, 43–48 (2021).
52. Govyadinov, A. A. et al. Probing low-energy hyperbolic polaritons in van der Waals crystals with an electron microscope. *Nat. Commun.* **8**, 95 (2017).
53. Kurman, Y. et al. Spatiotemporal imaging of 2D polariton wave packet dynamics using free electrons. *Science* **372**, 1181–1186 (2021).
54. Alfaro-Mozaz, F. J. et al. Nanoimaging of resonating hyperbolic polaritons in linear boron nitride antennas. *Nat. Commun.* **8**, 15624 (2017).
55. Nikitin, A. Y. et al. Real-space mapping of tailored sheet and edge plasmons in graphene nanoresonators. *Nat. Photon.* **10**, 239–243 (2016).
56. Wu, C., Salandrino, A., Ni, X. & Zhang, X. Electrodynamical light trapping using whispering-gallery resonances in hyperbolic cavities. *Phys. Rev. X* **4**, 021015 (2014).

Methods

Sample preparation for the TEM experiments

Thick (radii ≈ 20–50 nm) and thin (radii ≈ 2–10 nm) BNNT samples were synthesized using a previously reported method[57,58]. The final BNNT products were then dispersed in pure ethanol using an ultrasonic oscillator for 30 minutes for each product. Subsequently, three droplets of each solution were transferred onto 3 mm lacy carbon TEM grids. BNNTs were suspended on lacy carbon TEM grids. Before performing STEM measurements, the samples were annealed at 160 °C for 8 hours in a vacuum chamber to remove any possible hydroxide contamination.

AFM-IR experiment

NanoIR spectra were acquired using a commercial instrument (nanoIR3, Bruker Nano) that consisted of an AFM microscope operating in contact mode and a tunable pulsed laser source[40,42]. The pulsed laser repetition rate and cantilever decay signal were optimized at second contact oscillation frequency (~360 kHz) of the AFM tip. After optimizing the laser signal, nanoIR spectra were collected from 780 to 1,900 cm^{-1} at ~3 cm^{-1} intervals. The spatial resolution depended on the radius of curvature of the AFM tip, which was around 20 nm in our experiments.

The s-SNOM experiment

Near-field imaging was performed using a commercially available s-SNOM set-up (Neaspec) equipped with different infrared lasers. A metalized cantilever atomic force microscope tip served as a scattering near-field probe. The tip oscillated vertically at the mechanical resonance frequency of the cantilever (approximately 270 kHz) with an amplitude of approximately 50 nm. The tip was illuminated with monochromatic p-polarized infrared light from a quantum cascade laser. Using this technique, the tip-launched polaritons were reflected at the edges and produced polariton interference, as shown in Fig. 2c,d.

EELS and TEM imaging experiments

We carried out EELS experiments on a Nion U-HERMES200 TEM instrument equipped with a monochromator that was operated at 60 kV to avoid damage to BN materials. We employed a convergence semi-angle $\alpha = 20$ mrad and a collection semi-angle $\beta = 25$ mrad for all datasets. In this setting, the spatial resolution was ~0.2 nm, while the energy resolution was ~7.5 meV, suitable for the characterization of BNNTs. Moreover, the e-beam current used for EELS was ~10 pA, while the acquisition times were 200 ms per pixel and 500 ms per pixel for the separately measured datasets along directions parallel and perpendicular to the axis of the BNNTs. The zero-loss peak was slightly saturated to improve the signal-to-noise ratio of the spectra. The high-resolution TEM images in Fig. 1a and Supplementary Fig. 1 were obtained using an FEI Tecnai F20 TEM instrument operated at 200 kV.

EELS data processing

All the acquired vibrational spectra were processed using a custom-written MATLAB code and the Gatan Microscopy Suite. More specifically, the EELS spectra were first aligned by their normalized cross-correlation and then normalized to the intensity of the zero-loss peak. Subsequently, the block-matching and three-dimensional filtering (BM3D) algorithms were applied to remove Gaussian noise. The background arising from the tail of the zero-loss peak was fitted to a modified Peason-VII function with two fitting windows and then subtracted to obtain a cleaner vibrational signal. The Lucy–Richardson algorithm was subsequently employed to reduce the broadening effect induced by the finite energy resolution of the instrument, taking the elastic zero-loss peak as the reference point for the spread function. The so-processed spectra were summed along the direction parallel to the interface for obtaining line-scan data with a good signal-to-noise ratio. In addition, we employed a multi-Gaussian peak fitting method to extract the polariton peaks from the composed signal.

Theoretical calculations

The finite-element method implemented in Comsol Multiphysics is used to simulate the EELS spectra. Specifically, we numerically solve Maxwell's equations to evaluate the electric field $\mathbf{E}(\mathbf{r},t)$ produced by a moving electron in the presence of a BNNT, which is described by means of the dielectric function detailed in Supplementary Fig. 2 and Supplementary Note 1. By following a well-established procedure[59], a current source is used to represent the e-beam along the direction perpendicular to the sample[60,61]:

$$\mathbf{j}(\mathbf{r},\omega) = -e\dot{z}\delta(x-x_0)\,\delta(y-y_0)\exp(i\omega z/v), \tag{1}$$

where the electron is treated as a point charge $-e$ moving with constant velocity v along z and hitting the sample at the position $\mathbf{r}_0 = (x_0, y_0, 0)$ at time $t = 0$. We work in angular-frequency space ω and aim at obtaining the probability for the electron to lose an amount of energy $\hbar\omega$. The fast electron supplies an external evanescent field $\mathbf{E}^0(\mathbf{r},t)$ as it moves in vacuum, while the interaction with the sample induces a field $\mathbf{E}^{\mathrm{ind}}(\mathbf{r},t) = \mathbf{E}(\mathbf{r},t) - \mathbf{E}^0(\mathbf{r},t)$. Although $\mathbf{E}^0(\mathbf{r},t)$ is analytical, we calculate both $\mathbf{E}(\mathbf{r},t)$ and $\mathbf{E}^0(\mathbf{r},t)$ numerically, preserving the same mesh to increase the accuracy in the subtraction. The EELS probability is then obtained from the induced field as[48]

$$\Gamma_{\mathrm{EELS}}(\omega) = \frac{e}{\pi\hbar\omega}\int \mathrm{d}z\,\mathrm{Re}\left\{\exp(-i\omega z/v)\,E_z^{\mathrm{ind}}(x_0,y_0,z,\omega)\right\}. \tag{2}$$

We apply equation (2) to electrons passing near or through a BNNT and obtain the results presented in Supplementary Fig. 6. For a quantitative comparison with experiment, we incorporate the spectral resolution determined by the measured zero-loss peak (ZLP), so that we convolute the calculated spectra in Supplementary Fig. 6 with a Gaussian function (Supplementary Note 1 for details) according to

$$\Gamma_{\mathrm{EELS}}^{\mathrm{broadened}}(\omega) = \int \mathrm{d}\omega'\,\Gamma_{\mathrm{EELS}}(\omega-\omega')\,\mathrm{ZLP}(\omega'). \tag{3}$$

The so-broadened calculated probability, plotted in Supplementary Fig. 6, is in excellent agreement with the experiment.

Data availability

The data that support the findings of this study are available within the paper and the Supplementary Information. Other relevant data are available from the corresponding authors upon reasonable request. Source data are provided with this paper.

Code availability

The codes that support the findings of this study are available from the corresponding authors upon reasonable request.

References

57. Zhi, C., Bando, Y., Tan, C. & Golberg, D. Effective precursor for high yield synthesis of pure BN nanotubes. *Solid State Commun.* **135**, 67–70 (2005).
58. Huang, Y. et al. Bulk synthesis, growth mechanism and properties of highly pure ultrafine boron nitride nanotubes with diameters of sub-10 nm. *Nanotechnology* **22**, 145602 (2011).
59. García de Abajo, F. J. Optical excitations in electron microscopy. *Rev. Mod. Phys.* **82**, 209–275 (2010).
60. Raza, S. et al. Extremely confined gap surface-plasmon modes excited by electrons. *Nat. Commun.* **5**, 4125 (2014).
61. Konečná, A. et al. Vibrational electron energy loss spectroscopy in truncated dielectric slabs. *Phys. Rev. B* **98**, 205409 (2018).

Acknowledgements
This work was completed especially for the 20th anniversary of the National Center for Nanoscience and Technology, Beijing, China. This work was also supported by the National Key R&D Program of China (2021YFA1201500 to Q.D.; 2021YFA1400500 to E.-G.W.), the National Natural Science Foundation of China (51925203 and U2032206 to Q.D.; 52022025 and 51972074 to X.Y.; 52102160 to X.G.; 52125307, 11974023, 52021006 and T2188101 to P.G.), the Strategic Priority Research Program of the Chinese Academy of Sciences (XDB30000000 to X.Y.; XDB36000000 to Q.D.), the Youth Innovation Promotion Association of the Chinese Academy of Sciences (to X.Y.), the Open Project of Nanjing University (M34034 to Q.D.), the '2011 Program' from the Peking-Tsinghua-IOP Collaborative Innovation Center of Quantum Matter (to P.G.) and the Special Research Assistant Program of the Chinese Academy of Sciences (to X.G.). We also acknowledge the Electron Microscopy Laboratory of Peking University for the use of electron microscopes. F.J.G.d.A. acknowledges support from H2020 European Research Council (ERC) (advanced grant 789104-eNANO), Spanish Ministry for Science and Innovation (MCINN) (PID2020-112625GB-I00 and CEX2019-000910-S) and the Catalan Centres de Recerca de Catalunya (CERCA) Program. In addition, we express our gratitude to X. Zhang (Peking University) and S. Zhang (National Center for Nanoscience and Technology) for their help in sample preparation and characterization.

Author contributions
The concept for the experiment was initially developed by Q.D., X.Y. and P.G. Hexagonal BN nanotubes were grown by Y.H.; AFM-IR and s-SNOM experiments were performed by X.G. under the direction of Q.D.; STEM–EELS and TEM imaging experiments were performed by N.L. under the direction of P.G. and E.-G.W.; finite-element-method simulations and theoretical analysis were performed by X.G. under the supervision of Q.D., X.Y. and F.J.G.d.A.; data processing was performed by X.G. and N.L., assisted by C.W., R.Q., Y.L. and R.S.; X.G., X.Y. and Q.D. wrote the manuscript with advice from F.J.G.d.A. and P.G. All authors discussed the results at all stages and participated in the development of the manuscript.

Competing interests
The authors declare no competing interests.

Additional information
Supplementary information The online version contains supplementary material available at https://doi.org/10.1038/s41565-023-01324-3.

Correspondence and requests for materials should be addressed to Xiaoxia Yang, F. Javier García de Abajo, Peng Gao or Qing Dai.

Peer review information *Nature Nanotechnology* thanks Min Seok Jang and the other, anonymous, reviewer(s) for their contribution to the peer review of this work.